
Article:
Muangtong, P., Rodchanarowan, A., Chaysuwan, D. et al. (2 more authors) (2020) The corrosion behaviour of CoCrFeNi-x (x = Cu, Al, Sn) high entropy alloy systems in chloride solution. Corrosion Science, 172. 108740. ISSN 0010-938X

https://doi.org/10.1016/j.corsci.2020.108740

The corrosion behaviour of CoCrFeNi-x (x = Cu, Al, Sn) high entropy alloy systems in chloride solution

Piyanut Muangtong[a,b], Aphichart Rodchanarowan[c*], Duangrudee Chaysuwan[c], Narong Chanlek[d], Russell Goodall[a*]

[a]Department of Materials Science and Engineering, Faculty of Engineering, The University of Sheffield, Sheffield, Sir Robert Hadfield Building, Mappin St., S1 3JD, United Kingdom

[b]Department of Materials Engineering, Faculty of Engineering, Rajamangala University of Technology Rattanakosin, 96 Phutthamonthon Sai 5 Rd., Salaya, Phutthamonthon, Nakhon Pathom, 73170, Thailand

[c]Department of Materials Engineering, Faculty of Engineering, Kasetsart University, 50 Ngamwongwan Rd., Ladyaow, Chatuchak, Bangkok, 10900, Thailand

[d]Synchrotron Light Research Institute, Nakhon Ratchasima, 111 University Avenue, Muang District, 30000, Thailand

*r.goodall@sheffield.ac.uk and *fengacrw@ku.ac.th

Keywords: High-entropy alloys; Complex concentrated alloys; CoCrFeNi alloy; Corrosion resistance; Chloride solution.

Abstract

The corrosion properties in NaCl solution of four equiatomic HEAs of the CoCrFeNi system adding Al, Cu and Sn are investigated. These alloys are processed by vacuum arc melting and assessed via the Potentiostat method. The properties were compared with two standard stainless steels. The results indicate that CoCrFeNiSn possesses the best passivation in this solution, explained by the alloy phases and presence at the surface of elements in oxidation states corresponding to stable oxide films. The other systems show a range of behaviours attributable to their different microstructures and varying potential for stable oxide formation.

1. Introduction

Marine applications for structural alloys usually mean a high chloride environment which can lead to pitting corrosion, the localized formation of small holes at the surface. This can cause structural damage, and can contribute to mechanical failure, all the more serious as its initiation and propagation cannot be observed by normal visual inspection [1-4]. Such corrosion can have a serious impact in terms of risk to human life, economy and the environment, and it is fortunate that there are a wide range of options for preventing corrosion; for example, the use of coatings [1,5], inhibitor protection [1,6], cathodic protection [1,7] and the introduction of alloying elements to generate a stable native oxide [1,8,9]. Stainless steels

are well-accepted alloys for use in corrosive conditions due to their high Cr content (12-18%), which generates a surface oxide film and leads to reduced corrosion attack on the surface [1,10,11]. Recently however, there has been the discovery of new alloys which have chemical compositions of similar nature to stainless steels, which have better corrosion (or other) properties than conventional alloys.

This new type of alloy is called High Entropy Alloys (HEAs), also known as Complex Concentrated Alloys (CCAs). Originally, HEAs were taken to be alloys with single phase structure, though the breadth of research now encompasses several terms, and also alloys which are not equiatomic in composition, and which can be multiphase in structure [12,13]. In current usage, HEAs are multicomponent alloys with generally few solid solution phases of simple structure (such as body-centered cubic (BCC), face-centered cubic (FCC), or hexagonal close packed (HCP)) [14-17]. HEAs have been reported to have unusual properties of many types (including corrosion, mechanical, thermal and electrical properties, and wear properties [15-23]), and these behaviours suggest the potential for use in numerous applications, including nuclear, aerospace, energy, chemical, electronics, and marine infrastructure [15,17,24,25]. In particular, several HEA systems have been reported to show improved corrosion properties. An example is CoCrFeNi which has a wide passive region and low corrosion current density in 0.6M chloride solution as a result of a single solid solution phase and high Cr-oxide film [9,17]. $Co_{1.5}CrFeNi_{1.5}Ti_{0.5}Mo_{0.1}$ has a high pitting potential and low corrosion current density in 1M chloride solution owing to Mo-oxide on the sample surface [26]. FeCoCrAlNiTi has low corrosion current density in 3.5% chloride solution as a consequence of the increased oxide film formation due to the Ti addition [15]. Because of this, the CoCrFeNi system has attracted the most interest for the improvement in corrosion resistance in different solutions with the addition of other metallic elements, such as Al, Cu, Mo, and Ti [9,17,24,25,27]. However, a systematic comparison of different HEAs of these types is currently lacking. In particular, as pointed out in Ref. [28], as well as comparison across different alloys with the same conditions being lacking, there is also a need for advanced characterization of surface films to properly interpret the behaviours seen.

This paper therefore reports the results of an investigation of the corrosion resistance in aerated 0.6M chloride solution of the CoCrFeNi system, and the same base alloy with additions of a series of fifth elements known to generate changes in the microstructure, Al, Cu and Sn. These are relatively low-cost materials and so produce alloys that are potentially tractable for applications. Furthermore, the additional of Al is known to produce a single phase BCC alloy in the as cast state, in contrast to the FCC single phase structure of as cast CoCrFeNi [23], while Cu produces a two phase structure [22], as does the system with Sn [35], though this is somewhat less well reported in the literature. The behaviour is investigated electrochemically and the corrosion surfaces are explored to understand the changes occurring, and to link the properties to the composition and microstructure differences. The data and understanding will allow evaluation of such materials for use in industrial applications which require structural materials to operate under the risk of corrosion, such as submarine pipeline in the petroleum industry.

2. Materials and experiments

2.1 Materials

Raw materials consisted of seven elements; Co, Cr, Fe, Cu (Alfa Aesar, UK), Ni, Sn (Advent Research Materials, UK), and Al (Goodfellow, UK) at 99.95% purity or better. Specimens were made at equiatomic ratios of four alloys; CoCrFeNi, CoCrFeNiAl, CoCrFeNiCu, and CoCrFeNiSn. CoCrFeNi was the base composition with either no addition or the inclusion of Al, Cu, or Sn, as shown in Table 1. In addition, samples of the conventional alloys stainless steel grade 304 and 316 (SS304 and SS316) were processed by the same techniques from pre-alloyed material for comparison.

Table 1
The nominal and actual chemical compositions of the HEA specimens, the latter determined from EDS analysis.

HEA systems		Chemical composition (at.%)						
		Co	Cr	Fe	Ni	Al	Cu	Sn
CoCrFeNi	Nominal	25	25	25	25	-	-	-
	Actual	25.47	25.13	25.15	24.24	-	-	-
CoCrFeNiAl	Nominal	20	20	20	20	20	-	-
	Actual	20.67	20.54	20.46	19.93	18.39	-	-
CoCrFeNiCu	Nominal	20	20	20	20	-	20	-
	Actual	19.94	20.65	19.87	19.80	-	19.75	-
CoCrFeNiSn	Nominal	20	20	20	20	-	-	20
	Actual	20.71	18.73	20.31	19.82	-	-	20.42

The four HEA systems were created by the vacuum arc melting method (MAM1 arc melter, Buehler), re-melted five times [29,30], and cast into a cylindrical copper mold of 0.6 cm diameter. Subsequently, specimens were cut as cylinders as 6 mm in diameter × 10 mm height and the sample surface was ground and polished from a low number of grit paper down to 1 micron diamond suspension.

2.2 Experiments

2.2.1 Electrochemical set-up for corrosion study

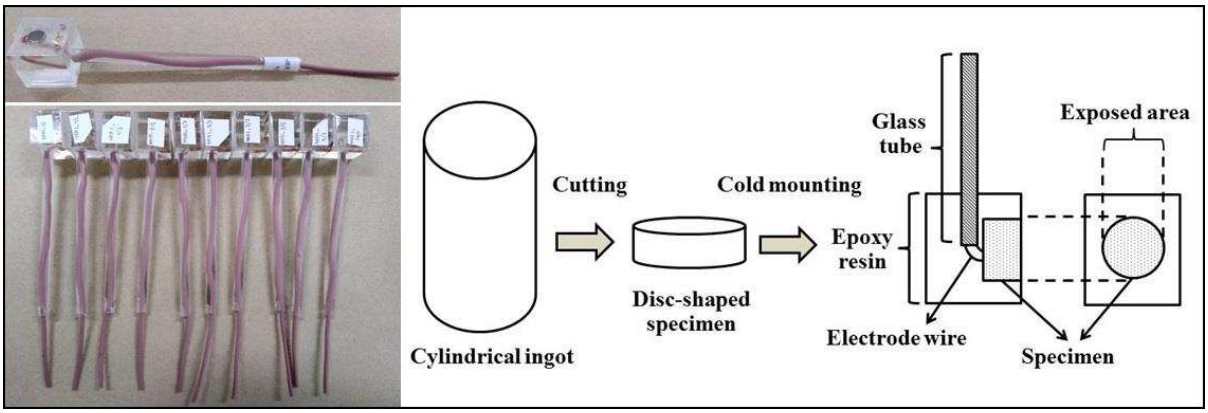

Fig. 1. The process of corrosion specimen preparation and the final specimens used.

The corrosion behaviour was studied by electrochemical analysis (PGSTAT302N Autolab, Metrohm Autolab). Corrosion specimens were electrically connected by a copper wire inserted in a glass tube and later mounted by epoxy resin in cubic silicone molds [31] as shown in Fig. 1. The exposed area of the sample to the solution was 0.28 cm^2 in each case. Three electrode cells were used for the corrosion investigation. The working, counter and reference electrodes were the prepared specimen, a platinum electrode, and Ag/AgCl reference electrode, respectively. The electrolyte used in this study was 0.6M NaCl solution [32] with a pH range from 7.65 to 7.99 at room temperature, in which each type of alloy was tested at least three times [33]. The scan rate used for the linear polarization was 1 mV/s [32]. The corrosion parameters, corrosion potential (E_{corr}), pitting potential (E_p), and passivation potential (ΔE_p), were analyzed after data collection by Nova 1.11.2 software.

2.2.2 Chemical and microstructural characterization

Contamination on the specimen surface after corrosion experimentation was avoided by cleaning with deionized water and isopropanol in an ultrasonic bath for 10 min before testing by other techniques. The phase composition of the samples was analyzed by X-ray diffraction (XRD; D2 Phaser, Bruker) over 2θ angles in the range 20-100 degrees at a scan rate of 2 deg/min [27,34]. The microstructure was observed with Scanning Electron Microscopy (SEM; Inspect F50, FEI) in backscattered electron (BSE) mode with Energy Dispersive Spectroscopy (EDS) for elemental detection on the specimen surface. The analysis of phase fraction on the sample surfaces was performed on a series of BSE images obtained from different locations for each alloy, and was carried out by using ImageJ software with analysis areas of 100 µm × 86 µm. In addition, the passive film on the sample surfaces was analyzed by X-ray Photoelectron Spectroscopy (XPS; PHI5000 Versa Probe II, Ulvac-PHI). The analysis area was set by a X-ray beam size of 100 µm diameter. Before the analysis, the sample surface was cleaned by Ar sputtering controlled not to exceed 10 nm in depth. Finally, cross-sections through particular surface features of interest in the HEA samples were obtained through Focused Ion Beam milling (FIB; Helios NanoLab G3 UC, FEI) after the sputtering a gold coating of 10 nm thickness (Q150T ES, Quorum). Cross sections were imaged by SEM to explore the relationship of these features to the microstructure of the alloy.

3. Results

3.1 As cast alloys

As shown in Fig. 2, the analysis of the XRD results indicates that the CoCrFeNi alloy consists of a single solid solution FCC phase, with, as expected, peaks consistent with $Cr_{0.25}Fe_{0.25}Co_{0.25}Ni_{0.25}$ (ICDD card number: 04-018-7506). The addition of a fifth alloying element either leads to the evolution of a second phase, resulting in a two phase structure, or to the formation of a new single phase. Of the first type, the Al addition transforms the phase from an FCC to BCC form (ICDD card number: 04-018-5047) with CoCrFeNiAl forming the ordered B2 phase with BCC structure. For the second type of effect, Cu and Sn additions lead to the formation of a two phase structure; CoCrFeNiCu shows segregation of elemental Cu (ICDD card number: 04-009-2090) from the major FCC phase present in CoCrFeNi, and

CoCrFeNiSn retains the FCC structure of CoCrFeNi and introduces a hexagonal structure with similar peaks to $Ni_{1.5-1.63}Sn$ (ICDD card number: 04-017-6375 and 04-016-8768).

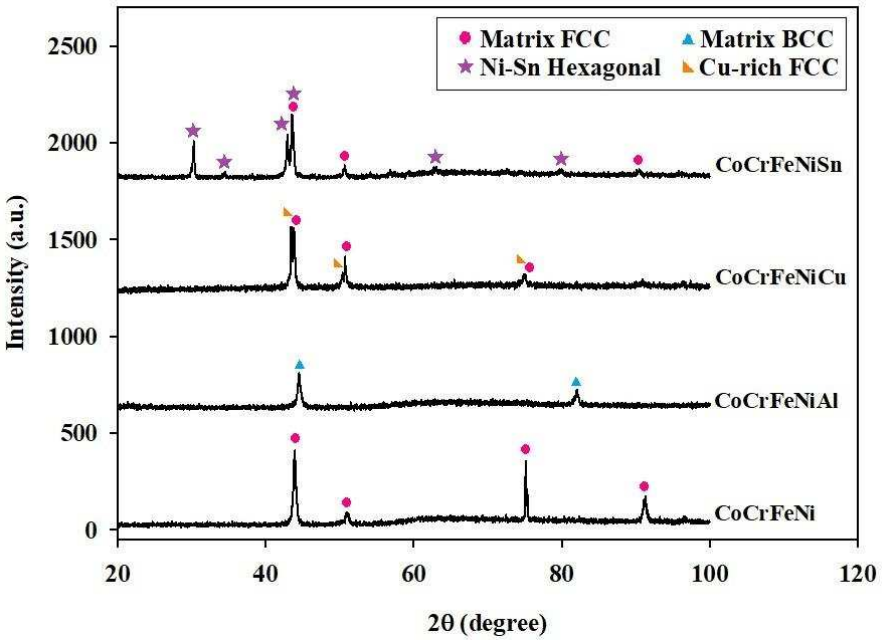

Fig. 2. The XRD patterns of the four HEA samples examined, in the as-cast form.

This phase evolution of the HEA systems studied is in accord with previous literature [33-37]. It has been suggested that the phase transformation of CoCrFeNiAl alloys stems from the different atomic size between the elements of the CoCrFeNi system and Al, which is larger [33,34], though more comprehensive descriptions or alloys would use the relative energies of the electronic structure of different systems as a means to discriminate between different structures. Meanwhile, the addition of Sn as an alloying element leads to the formation of two phases, which is likely to be caused by the mixing enthalpy of different atomic pairs ($\Delta H_{mix,<ij>}$) in the system. The $\Delta H_{mix,<ij>}$ of the Ni-Sn couple has the most negative value, including strong bonding between these being preferred, and leading to the formation of Ni-Sn phase. Other possible couples (Co, Cr, Fe and Ni) with Sn have a positive $\Delta H_{mix,<ij>}$ value, indicating that these elements will not readily interact with the tin [35,36]. By similar reasoning, the influence of Cu on the increase in positive mixing enthalpy of CoCrFeNi system can give rise to Cu segregation in the HEA structure [37].

3.2 Corrosion analysis

The corrosion behaviour of samples immersed in 0.6M NaCl solution at room temperature is analyzed by linear polarization plots. Fig. 3 shows the plot of current density (i; A/cm^2) against potential (E; V vs. Ag/AgCl). Some of the HEA systems show good corrosion properties when compared with the conventional stainless steels as seen in Fig. 3. From these curves, the corrosion parameters such as corrosion potential (E_{corr}), pitting potential (E_p) and passivation potential ($\Delta E_p = E_p - E_{corr}$) can be extracted, as given in Table 2. Both E_p and ΔE_p are measured to indicate the extent of the passive region under medium chloride conditions.

These parameters help to reveal the corrosion-resisting capability of the oxide films during the electrochemical operation.

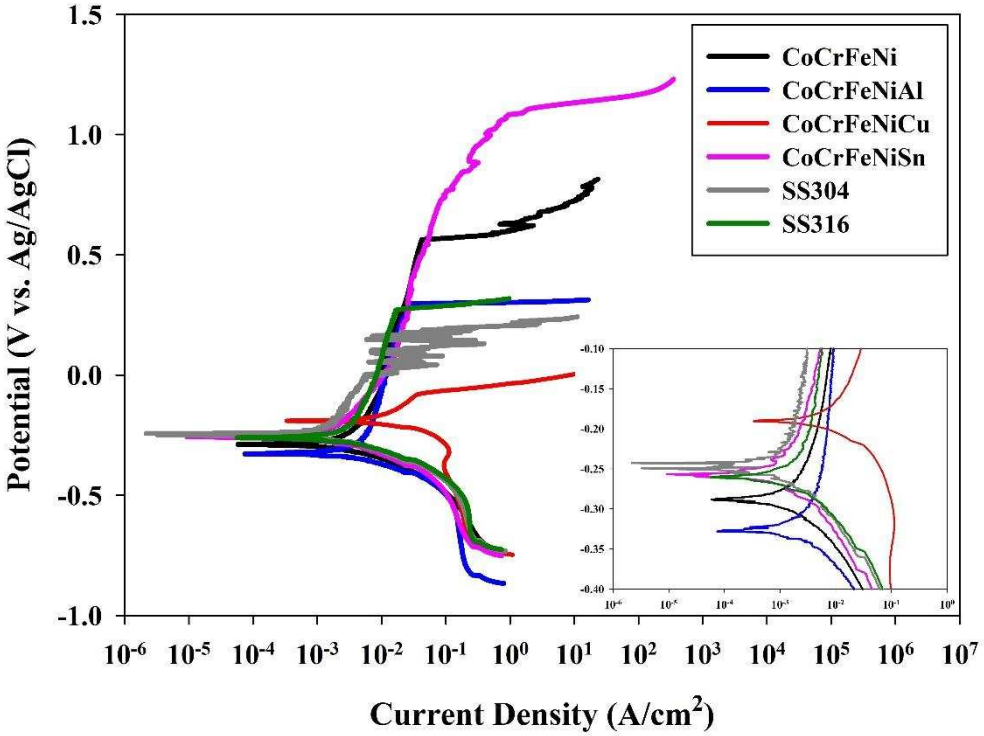

Fig. 3. Linear polarization curves of HEA and stainless steel samples immersed in 0.6M NaCl solution at room temperature.

Table 2

The corrosion properties of HEA and stainless steel samples immersed in 0.6M NaCl solution at room temperature.

Alloys	E_{corr} ($mV_{Ag/AgCl}$)	E_p ($mV_{Ag/AgCl}$)	ΔE_p ($mV_{Ag/AgCl}$)
CoCrFeNi	-257±13	556±27	813±30
CoCrFeNiAl	-322±10	297±40	619±43
CoCrFeNiCu	-180±13	-69±9	111±21
CoCrFeNiSn	-252±5	1099±14	1351±12
SS304	-246±13	199±12	445±17
SS316	-254±7	267±35	521±42

The CoCrFeNiSn system shows the best corrosion resistance compared to the other alloys since it shows the highest pitting potential and the largest passive region. The full values for this HEA, Table 2, show it has the highest ΔE_p, indicating good stability of the passive film in the pitting-corrosion region of the polarization test. The enhancement of the passive region must stem from the Sn addition, which could form a stable passive film at the surface and contributes to protecting the sample surface from chloride-ion attack. It can be observed that the alloy with the addition of Sn shows the widest passive region as seen in Fig. 3. In addition, CoCrFeNiSn shows the highest E_p and ΔE_p when compared with other alloys as seen in Table 2. This further indicates the formation of a strong oxide film in the CoCrFeNiSn system, which is resistant to corrosion attack and oxide-film breakdown.

In contrast, the lowest E_p and ΔE_p values are found in the alloy with Cu; this HEA has the highest E_{corr}, and was observed to have the narrowest passive region of the alloys examined here, Fig. 3 and Table 2. The Cu addition has the most negative effect on the corrosion properties, as evidenced by showing the lowest E_p and ΔE_p. Furthermore, CoCrFeNiCu and CoCrFeNiAl have lower corrosion resistance than the stainless steels, SS304 and SS316. The other two HEA systems, CoCrFeNi and CoCrFeNiSn have higher corrosion resistance than the stainless steels, having a large passive region in chloride solution.

3.3 Post-corrosion alloy microstructure and composition analysis

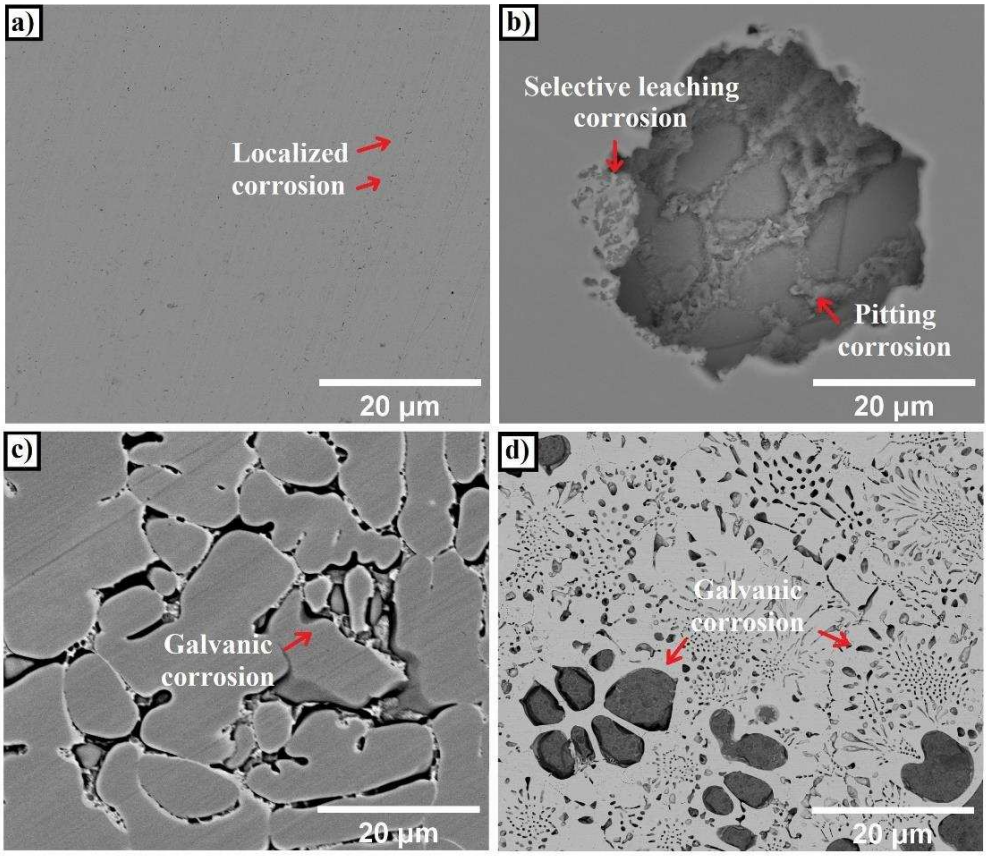

Fig. 4. BSE images of the surface of HEAs samples after immersion in 0.6M NaCl solution at room temperature; a) CoCrFeNi, b) CoCrFeNiAl, c) CoCrFeNiCu, and d) CoCrFeSn.

HEA samples were examined by SEM after being immersed in the chloride-containing solution. As shown in Fig. 4, BSE images reveal the HEA microstructures which have been damaged by chloride-ion attack. Localized corrosion of the CoCrFeNi surface is observed in Fig. 4a. This may have been initiated by chloride-ion attack in an area having low-Cr content, as some variation in composition in this alloy on an atomic scale has been observed in other work [35]; however it should be noted that with the sensitivity of the methods applied here no in homogeneity in element distribution was seen in CoCrFeNi. This shows that the passive films formed are relatively weakly bonded and insufficiently stable for restricting the propagation of corrosion in this system [9,27]. Fig. 4b shows the CoCrFeNiAl surface structure, exhibiting very large pitting holes, with another material or residue around their outer edge, sometimes filling the interior of smaller holes. Detailed examination indicates two types of

corrosion behaviour, an apparent selective leaching corrosion, leading to pitting corrosion once the product of selective leaching is removed. The surface damage after corrosion of the CoCrFeNiCu system is displayed in Fig. 4c. This alloy contains a matrix-FCC phase and a Cu-rich phase, which leads to the galvanic corrosion driven by the different potential of these phases [9]. Examination of the CoCrFeNiSn system shows a dendritic structure with a finer scale rod-like eutectic formed in the interdendritic regions. The structure consists of a Ni-Sn phase (brighter regions) and a CoCrFeNi-FCC phase (darker regions), Fig. 4d. Corrosion is seen to take place more significantly on the FCC phase, likely to stem from the different potential values of the two phases in the same manner (though to a lesser extent) as in the CoCrFeNiCu system [35,36].

Table 3

The results of phase fraction analysis via ImageJ software and the general surface characteristics of the HEA surfaces after corrosion testing.

Alloys	Phase composition	Phase fraction (%)	Surface characteristics
CoCrFeNi	FCC (CoCrFeNi)	100	Low corrosion
CoCrFeNiAl	BCC (CoCrFeNiAl)	100	High corrosion
CoCrFeNiCu	FCC (CoCrFeNi)	86.8 (±3.3)	Not corroded
	FCC (Cu-rich)	13.2 (±3.3)	Corroded
CoCrFeNiSn	Hexagonal (Ni-Sn)	63.8 (±4.1)	Not corroded
	FCC (CoCrFeNi)	36.2 (±4.1)	Corroded

The phase fraction and surface characteristics were analyzed from BSE images of the surface of the HEA samples using ImageJ software indicated the phase fraction of the different phases and the location of the most apparent corrosion as summarised in Table 3. In both CoCrFeNi and CoCrFeNiAl it was not possible to distinguish a second phase (in agreement with the earlier results indicating that these are single phase alloy, section 3.1). On the other hand, CoCrFeNiCu and CoCrFeNiSn both showed two distinct phases (also in agreement with the earlier results). In the CoCrFeNiCu alloy, the majority of the structure (more than 85%) was a CoCrFeNi- containing phase (FCC-structured from the XRD results), while the remainder was a phase heavily dominated by Cu. In the alloy of CoCrFeNiSn the dominant phase (more than 60%) was Ni-Sn (likely to be hexagonal from the XRD results), but there was a significant proportion of CoCrFeNi phase present as well. In the latter two alloys, where there were two phases present, it was also attempted to determine the scale of the microstructure. For the CoCrFeNiCu alloy, the Cu rich phase occurred at grain boundaries, forming interconnected networks that were typically 1-2 μm in thickness, but extended throughout the alloy. The CoCrFeNiSn appeared to show the CoCrFeNi phase on several scales, firstly in possibly dendritic structures of around 5-10 μm in diameter, and a finer eutectic-like structure at a submicron scale.

The images were also used to identify the extent of corrosion, and, for the two phase samples, whether this was more associated with a particular phase. It was found that CoCrFeNi has a lower corroded area than CoCrFeNiAl, even though both display a single phase. In the CoCrFeNiCu and CoCrFeNiSn systems, two phases are present. The Cu phase in CoCrFeNiCu

is the main phase corroded by chloride attack, while the CoCrFeNi has little apparent damage in this alloy. By contrast, the CoCrFeNi phase shows more extensive corrosion in CoCrFeNiSn, while the Ni-Sn phase does not appear to have been affected. This indicates that the Ni-Sn phase in the CoCrFeNiSn system probably has the best corrosion resistance of all the separate phases under these conditions of the materials investigated here. These observations correspond with the corrosion properties of HEAs in Table 2 and the corroded SEM images of HEAs in Fig. 4.

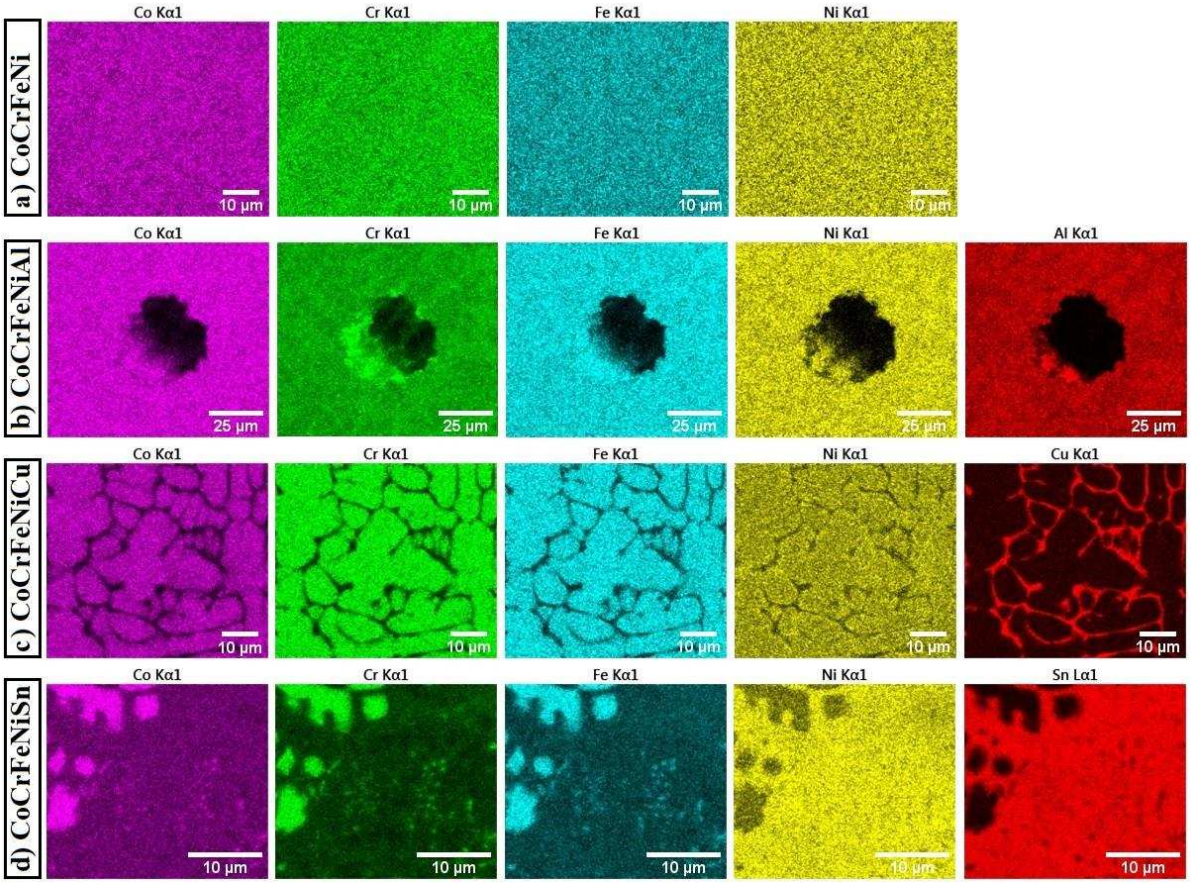

Fig. 5. EDS mapping images of the surface of HEAs samples after immersion in 0.6M NaCl solution at room temperature; a) CoCrFeNi, b) CoCrFeNiAl, c) CoCrFeNiCu, and d) CoCrFeNiSn.

The distribution of elements in the SEM images taken post corrosion testing was determined by EDS mapping, as shown in Fig. 5. The chemical distributions confirm the phase composition as assessed above and from XRD. It can be seen that there is (as measured by this technique) a homogeneous distribution of the constituent elements in the CoCrFeNi system Fig. 5a, which will be the single FCC phase. The CoCrFeNiAl system also shows a generally homogenous distribution (the defect in the center of the image is a corrosion pit), Fig. 5b, with some slight structure visible in the distribution of Cr, Ni and Al indicating separation between the former and latter of these elements. This structure will be the single BCC phase identified from XRD. The addition of Cu or Sn to the main HEA system leads to a non-uniform elemental distribution and the formation of two phases. CoCrFeNiCu, Fig. 5c, shows strong segregation of Cu way from the other elements, which are well-mixed. The Cu forms at the grain boundary regions, and correlates with the observed corrosion damage. In CoCrFeNiSn, the bright region on

the BSE image in Fig. 4d is associated with Ni and Sn, likely to be a hexagonal Ni_xSn intermetallic phase, in Fig. 5d while the other region can be confirmed as CoCrFeNi (the FCC phase).

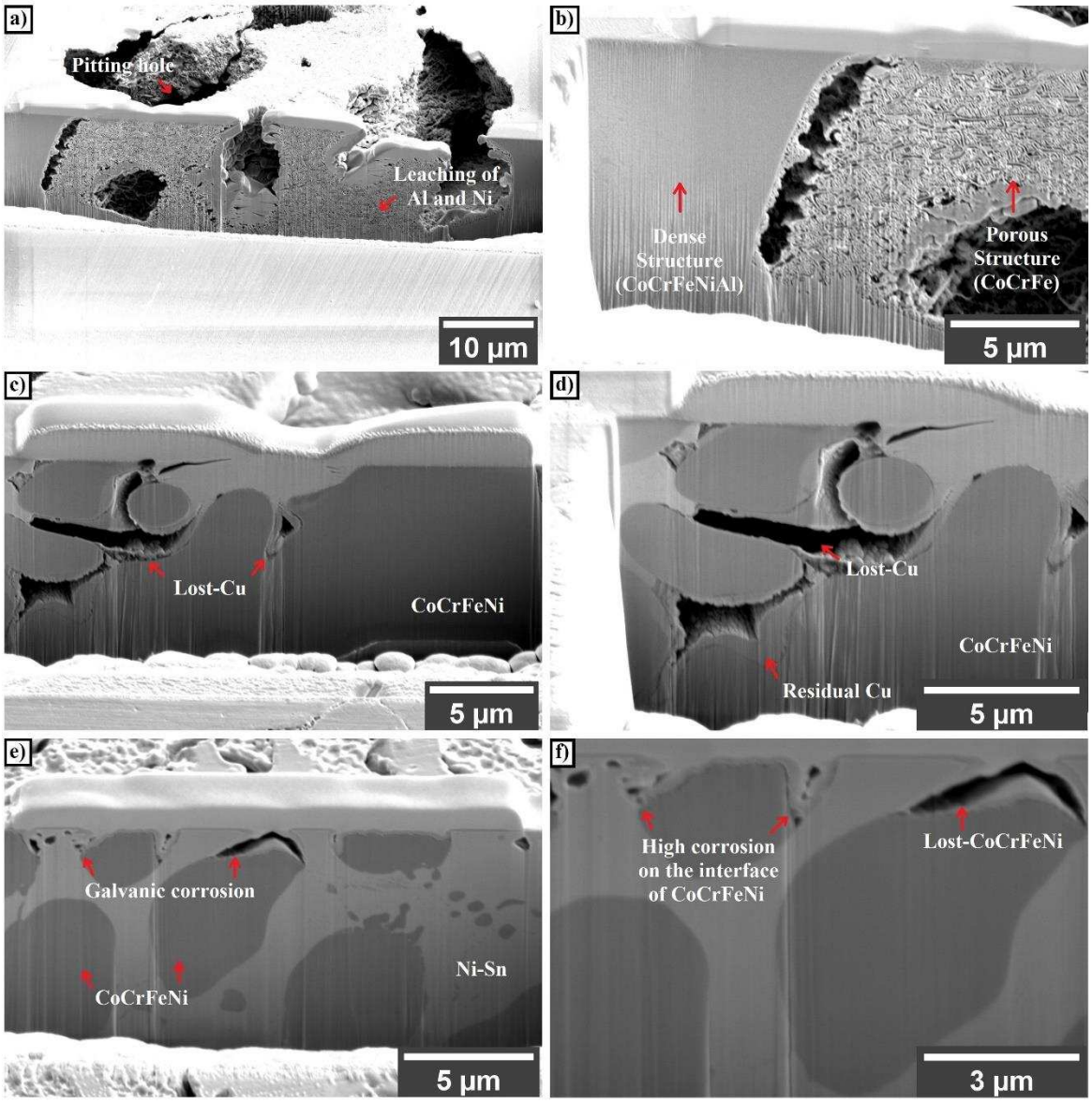

Fig. 6. Cross-sectional SEM images of FIB cross sections through features observed on the surface of HEA samples immersed in 0.6M NaCl solution at room temperature; a-b) CoCrFeNiAl, c-d) CoCrFeNiCu, and e-f) CoCrFeNiSn.

To explore the corrosion processes further, cross sections around particular features seen after corrosion in some of the samples were made with FIB and were imaged in the SEM, Fig. 6. CoCrFeNiAl, Fig. 6a and 6b, has two structures; one apparently porous which exists within other, larger cavities in the overall dense, unaffected structure; these larger cavities are also, sometimes vacant. The former of these is the first to be created in the corrosion process, and is likely to be the by-product of the selective leaching of two elements, Al and Ni (as shown by EDS maps, Fig. 7). The remaining Fe, Co and Cr take up less volume and reorganize into a porous structure during a dealloying process, as confirmed in Fig. 7.

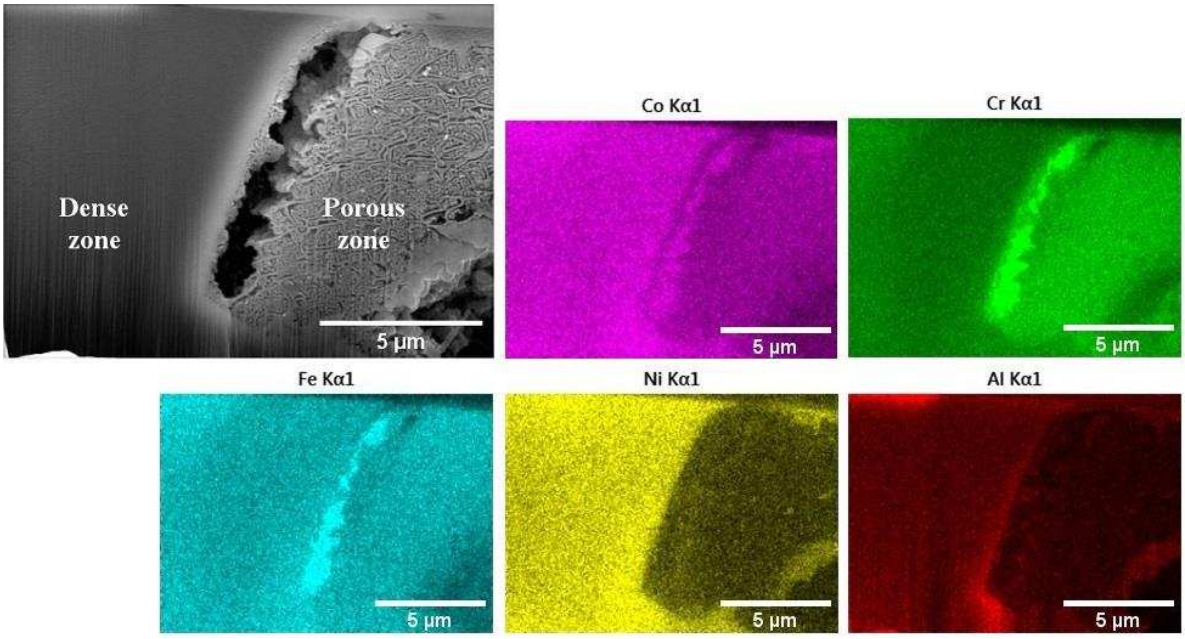

Fig. 7. EDS mapping images of cross-sectional CoCrFeNiAl immersed in 0.6M NaCl solution at room temperature.

Cross sectional SEM images of particular features identified on the surface of CoCrFeNiAl, CoCrFeNiCu, and CoCrFeNiSn were taken, and are shown in Fig. 6. The intent of these images was to explore if these features were associated with the underlying microstructure of each of these alloys (it should be noted that the resolution of the analysis used is not sufficient to offer information on the microstructure within the oxide films formed). The cross-sectional image of corrosion features seen on the surface of CoCrFeNi shows the interconnected distribution of the Cu phase, which is corroded to a large extent in comparison to the FCC phase in Fig. 6c and 6d, supporting the interpretation of this corrosion being galvanic origin. The cross sectional image of CoCrFeNiSn, Fig. 6e and 6f, shows attack of the CoCrFeNi phase in preference to the Ni-Sn phase. This is particularly high at the interface, as shown in Fig. 6f. It is again likely to be due to galvanic corrosion between FCC CoCrFeNi and the Ni-Sn phase.

3.4 Post-corrosion surface analysis

The oxide films formed on the HEA surfaces after the electrochemical experiment were analyzed by the XPS technique. This technique can determine chemical composition in the uppermost 5-10 nm of the sample surface and is, therefore, suitable for studying the passive film [33]. It should be noted that the method cannot, of course, elucidate the sub-nanometer structure of the oxide films produced, and a full analysis of this structure to assess the formation mechanisms and behavior during corrosion would require Transmission Electron Microscope observation, which is not performed here. The XPS survey spectra and high resolution XPS spectra in the binding energies range of 40-70 eV of HEA samples are shown in Fig. 8. The spectra reveal the presence of Co, Cr, Fe, Ni, O and C on all HEA sample surfaces. Additional peaks attributed to the presence of Al, Cu and Sn are observed on the CoCrFeNiAl, CoCrFeNiCu, and CoCrFeNiSn sample surfaces, respectively. The detection of C is possibly due to adventitious carbon contaminations. The presence of O suggests that an oxide film is formed on the sample surface, some metals being oxidized.

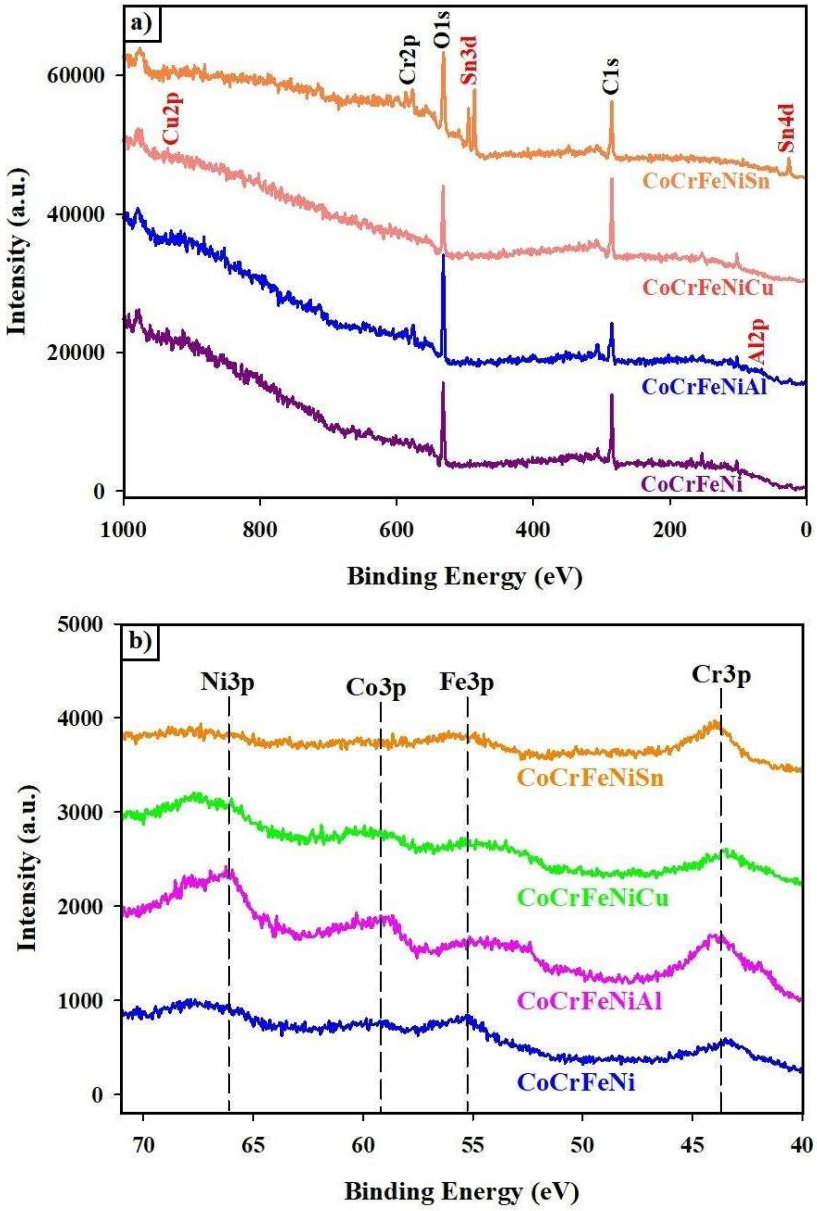

Fig. 8. a) XPS survey spectra and b) high resolution XPS spectra in the binding energies range of 40-70 eV of HEA samples after corrosion testing.

The relative atomic concentration of each element can be calculated by Eq. (1) and (2) [3,33].

$$X_i = 100 \frac{A_i}{\sum_{i=1}^{n} A_i} \quad (1)$$

where i refers to each element, n is the amount of elements, X_i is the atomic percent of each element, and A_i is the adjusted elemental intensities, which are obtained from

$$A_i = \frac{J_i}{S_i K} \quad (2)$$

where J_i is the measured intensity of each elemental composition, K is the kinetic energy, and S_i is the relative sensitivity which is determined from the XPS measurement.

Table 4

The chemical composition on the HEA sample surfaces after corrosion testing.

HEA systems	Relative atomic concentration (at.%)						
	Co	Cr	Fe	Ni	Al	Cu	Sn
CoCrFeNi	14.32	40.33	30.22	15.13	-	-	
CoCrFeNiAl	12.47	28.50	15.38	17.43	26.23	-	-
CoCrFeNiCu	14.09	29.50	16.79	18.82	-	20.80	-
CoCrFeNiSn	6.19	35.54	13.53	9.42	-	-	35.32

The calculated relative atomic concentrations of the HEA surface via XPS analysis are presented in Table 4. It is found that Cr is present at the surface in the highest proportion in all HEA systems; CoCrFeNi (40.33 at.%), CoCrFeNiSn (35.54 at.%), CoCrFeNiCu (29.50 at.%), and CoCrFeNiAl (28.50 at.%), while the proportion of the added alloying elements to the base CoCrFeNi are as follows; Sn/CoCrFeNiSn (35.32 at.%), Al/CoCrFeNiAl (26.23 at.%), and Cu/CoCrFeNiCu (20.80 at.%). In particular, it would be expected that Cr, and possibly the alloying elements, lead to the potential for forming an oxide layer on the sample surface and may participate in such a layer. Thus, they are the vital factor directly relating to the improvement in corrosion properties of HEA samples, and XPS can be further used to examine and compare the oxidation state of these elements at the surface. From this, with the assumption that these are bonding with oxygen, it can be inferred which elements are present in any oxide film that is formed. In the discussion that follows, to be concise we refer to the elements in their metallic state (e.g. Cr) and in the oxide corresponding to the oxidation state measured (e.g. Cr_2O_3); it must be noted however that the actual films formed are likely to mixtures of oxides of different elements. Detailed analysis of this by Transmission Electron Microscopy will take place in future work.

Fig. 9 shows the high resolution XPS spectra in the Cr 2p, Al 2p, Cu $2p_{3/2}$, and Sn 3d peak regions of HEA samples. The Cr 2p spectra of all the HEA samples exhibit two main spin-orbit peaks, Cr $2p_{3/2}$ and Cr $2p_{1/2}$, separated by approximately 9.6 eV. The Cr $2p_{3/2}$ peaks can be deconvoluted into two components at the binding energies of 574.12 eV and 576.60 eV-576.90 eV which are attributed to Cr and Cr^{3+} (Cr_2O_3), respectively. This indicates that Cr_2O_3 is formed to a large extent on all the HEA samples. The Al 2p peak of the CoCrFeNiAl sample can be fitted into two peaks at the binding energies of 72.39 eV and 74.58 eV corresponding to Al and Al^{3+} (Al_2O_3), respectively. The high Al_2O_3 content of 74.50 at.% is observed. The Cu $2p_{3/2}$ peak of CoCrFeNiCu sample exhibits two main peaks of Cu and Cu^{1+} (Cu_2O) at the binding energies of 932.68 eV and 933.70 eV, respectively, showing the low content of Cu_2O (18.26 at.%). The Sn $3d_{5/2}$ peak of CoCrFeNiSn can be fitted into two peaks at the binding energies of 484.80 eV and 486.39 eV which are attributed to Sn and Sn^{4+} (SnO_2), respectively. This suggests that SnO_2 is formed with high content of 86.47 at.%. The atomic proportions of metal oxides and metals are summarized again in Table 5.

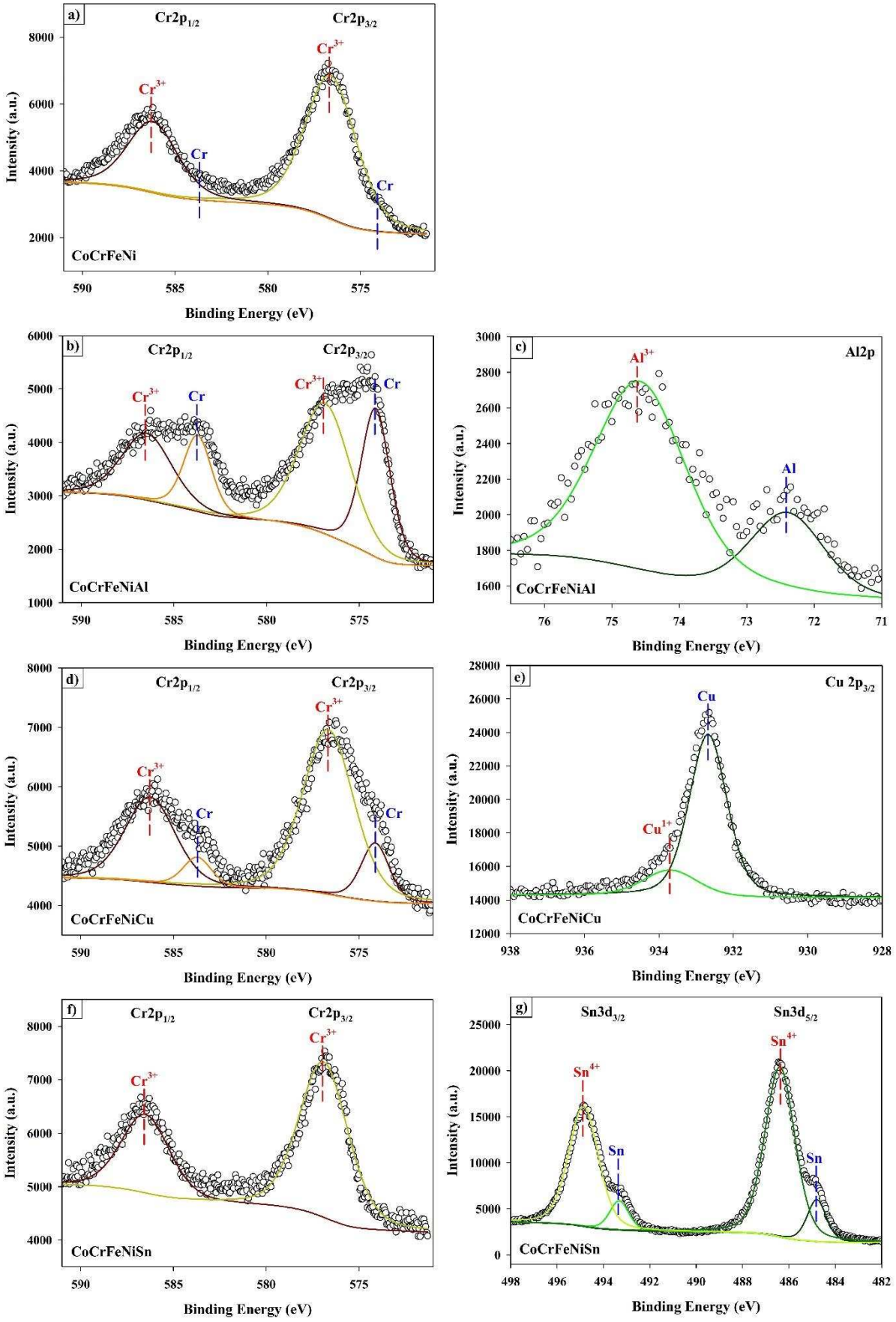

Fig. 9. High resolution XPS spectra in the; a,b,d,f) Cr 2p, c) Al 2p, e) Cu $2p_{3/2}$, and g) Sn 3d peak regions of HEA samples after corrosion testing.

Table 5

The relative atomic proportion of metal oxides and metals (referred to atomic percentage of the total content of the element at the surface) on the HEA sample surfaces after corrosion testing.

HEA systems	Cr (Cr at.%)		Al (Al at.%)		Cu (Cu at.%)		Sn (Sn at.%)	
	Cr^{3+}	Cr	Al^{3+}	Al	Cu^{1+}	Cu	Sn^{4+}	Sn
CoCrFeNi	99.85	0.15	-	-	-	-	-	-
CoCrFeNiAl	60.85	39.15	74.50	25.50	-	-	-	-
CoCrFeNiCu	83.62	16.38	-	-	18.26	81.74	-	-
CoCrFeNiSn	100.00	0.00	-	-	-	-	86.47	13.53

It can be seen from the results that the addition of Al and Cu have the effect of reducing the formation of Cr_2O_3 (more of the Cr is in the metallic state), while the oxide films which are generated by these alloying elements, Al_2O_3 and Cu_2O, are at moderate to low intensity Al_2O_3 (74.50 at.%) and Cu_2O (18.26 at.%). These oxide films are weakly bonded and unstable under the tested conditions, and thus lead to the poorer corrosion resistance observed in these alloys, being present at a lower proportion after corrosion testing [9,33]. Al_2O_3 is relatively weak at preventing chloride-ion attack, owing to chloride-ion adsorption through the oxide film [38], while Cu_2O is formed at low thickness; approximately 5 nm [39]. By contrast to these alloys, the addition of Sn results in an increase in proportion of conversion of metallic form to oxide for both Cr_2O_3 (100 Cr at.%) and SnO_2 (86.47 Sn at.%). This system can therefore form a significant passive film, which is stronger bonding than the other oxides formed on these alloys. XPS analysis confirms that there is the largest proportion of the passive film remaining after corrosion in the CoCrFeNiSn. The Cr_2O_3 is known to be a stable, corrosion-resistant oxide, and there is evidence to suggest that SnO_2 is also a stable film with high potential for protecting against chloride-ion attack [40,41].

4. Discussion

Following the evidence presented and discussed above, it is possible to propose a series of mechanisms for the corrosion in chloride solution of the HEAs examined in this work. In the CoCrFeNiAl system, it is found that pitting corrosion occurs, with a suggested mechanism for this, consistent with the observations here and what is known about the alloy shown in Fig. 10a-10c. The passive films, Cr_2O_3 and Al_2O_3, will be formed when the sample surface is in contact with atmospheric oxygen, as shown in Fig. 10a. Subsequently, during the corrosion process in Fig. 10b, there are three stages to the evolution of pitting; the first is the selective dissolution of Al and Ni from an area happening to be (Al-Ni)-rich (some tendency for this was seen in Fig. 5b). There areas form as the atomic pair of Al-Ni have the strongest enthalpy of formation in this system [32,42]. Corrosion proceeds by dealloying as Al has the lowest standard electrode potential and the Al_2O_3 is weak. The second, propagation step is the increasing damage in the region of the pits from small to large corrosion holes [28,33]. The final stage is when the CoCrFe residue from dealloying is removed from the hole, leaving behind the large corrosion pits seen. As indicated in Fig. 10c, repassivation of the oxide films may occur on the pitting holes after chloride-ion attack.

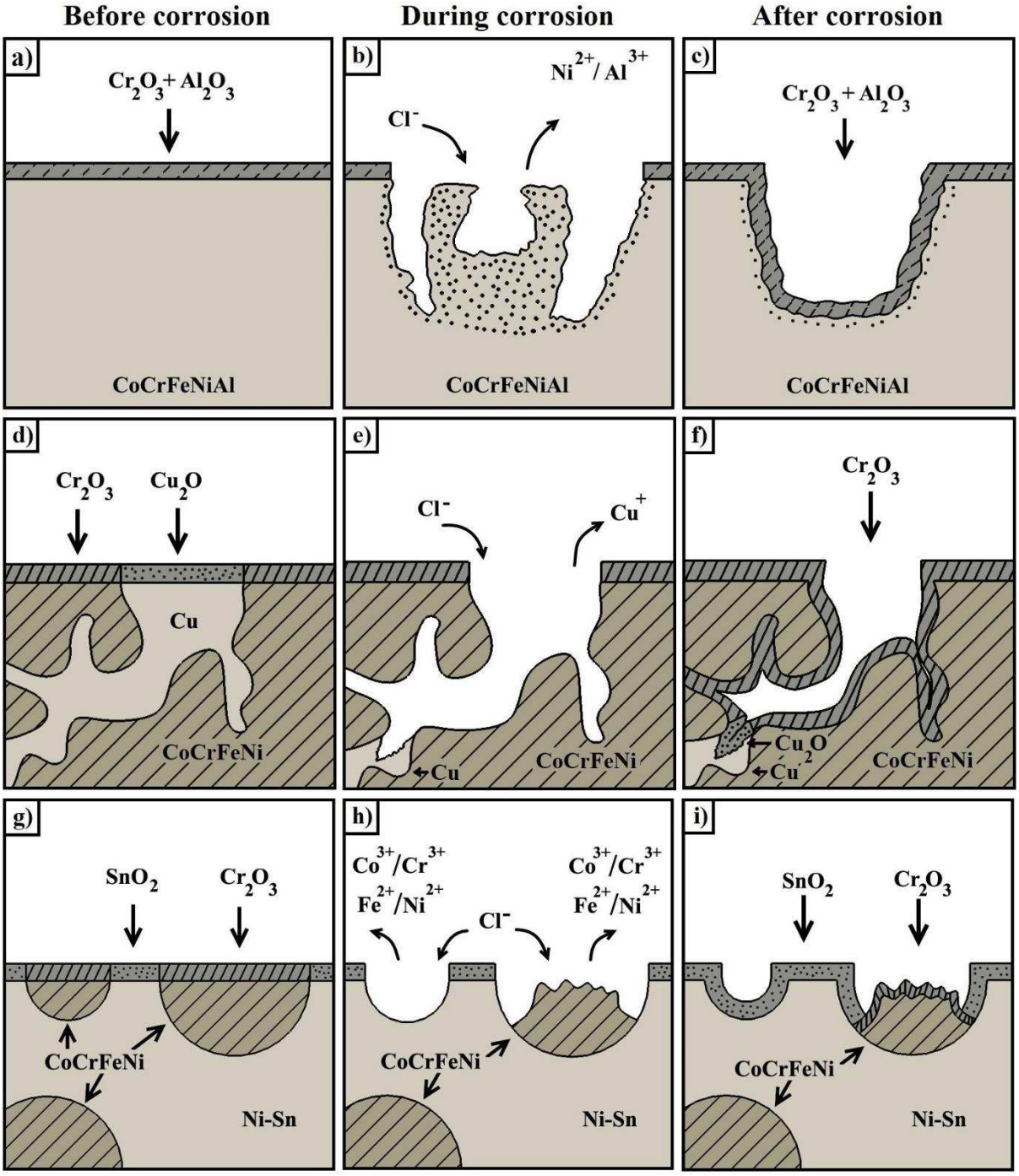

Fig. 10. A schematic diagram of the proposed processes occurring during the corrosion of some of the HEA samples examined in this work when tested in 0.6M NaCl solution at room temperature; a-c) CoCrFeNiAl, d-f) CoCrFeNiCu, and g-i) CoCrFeNiSn.

For the CoCrFeNiCu system, two oxide films are formed, Cr_2O_3 and Cu_2O, Fig. 10d. Cr_2O_3 is known to be a strong film, resistant to chloride attack, while Cu_2O is a weak film which easily breaks down in the presence of chloride ions. Fig. 10e shows the chloride ions attacking the Cu-rich areas, leading to the removal of Cu^{1+} from the main Cu phase. Galvanic corrosion of the segregated Cu phase occurs, stemming from its differing potential from the main FCC phase, which forms the cathode, with the Cu-rich phase acting as the anode [9]. The

Cu-rich phase is heavily corroded compared to the FCC phase. After corrosion, oxide layers may be regenerated on the sample surface, especially in the areas with Cr, Fig. 10f.

The corrosion behavior of CoCrFeNiSn is depicted in Fig. 10g-10i. The bulk microstructure of this alloy is composed of two phases, a Ni-Sn intermetallic and CoCrFeNi, which form two passive films, SnO_2 and Cr_2O_3 respectively. Both of these are a noble oxide films and will inhibit corrosion in chloride solution, as presented in Fig. 10g. Galvanic corrosion is observed on the FCC phase (indicating the Ni-Sn phase has a higher corrosion potential than the CoCrFeNi phase), particularly at the interface where the damage is relatively high, and as a result there is dissolution of some ions, Co^{3+}, Cr^{3+}, Fe^{2+}, and Ni^{2+}, as shown in Fig. 10h. Then the two passive films can regenerate, as shown in Fig. 10i.

In general, it should be noted that the mechanisms proposed for corrosion depicted in Fig. 10 are all based on the assumption that the oxide films have a simple structure of good uniformity; local variations and defects (which have not been explored here) could contribute to additional behaviors.

To sum up, the addition of Sn has a positive effect on the rise in corrosion resistance of equiatomic CoCrFeNi in a medium chloride-containing solution, while Al and Cu as alloying elements lead to the decline in corrosion properties under the same conditions.

5. Conclusions

CoCrFeNiSn has the largest passive region under the chloride attack conditions used, compared with the other alloys tested here, CoCrFeNi, CoCrFeNiAl, CoCrFeNiCu and stainless steel 316 and 304. This arises as the result of two conditions; the extensive formation of stable Cr_2O_3 and SnO_2 films on the sample surface, while the other novel alloys tested here show unstable passive films, and the particular phase formation in this system (particularly the occurrence of a Ni-Sn phase). Although the structure and composition of the oxides formed locally on the different phases could benefit from TEM study, to be performed in future work, the indications of this investigation are that the CoCrFeNiSn alloy may be a candidate for applications where structural materials capable of surviving marine or other chloride rich environments are needed.

Acknowledgements

Authors acknowledge the Royal Thai Government for the financial support including the Synchrotron Light Research Institute and Department of Materials Engineering, Faculty of Engineering, Kasetsart University, Thailand for the instrumental support for this project. RG would like to acknowledge a Fellowship supported by the Royal Academy of Engineering under the RAEng/Leverhulme Trust Senior Research Fellowships scheme.

Data Availability Statement

The raw and processed data required to reproduce these findings cannot be shared at this time as the data also forms part of an ongoing study.

References

[1] Z.H. Jin, H.H. Ge, W.W. Lin, Y.W. Zong, S.J. Liu, J.M. Shi, Corrosion behaviour of 316L stainless steel and anti-corrosion materials in a high acidified chloride solution, Appl. Surf. Sci. 322 (2014) 47-56. https://doi-org.sheffield.idm.oclc.org/10.1016/j.apsusc.2014.09.205

[2] B. Zhang, Y. Zhang, S.M. Guo, A thermodynamic study of corrosion behaviors for CoCrFeNi-based high-entropy alloys, J. Mater. Sci. 53 (2018) 14729-14738. https://doi-org.sheffield.idm.oclc.org/10.1007/s10853-018-2652-2

[3] Y. Shi, L. Collins, N. Balke, P.K. Liaw, B. Yang, In-situ electrochemical-AFM study of localized corrosion of $Al_xCoCrFeNi$ high-entropy alloys in chloride solution, Appl. Surf. Sci. 439 (2018) 533-544. https://doi-org.sheffield.idm.oclc.org/10.1016/j.apsusc.2018.01.047

[4] S. Street, N. Mi, A. Cook, H. Mohammed-Ali, L. Guo, T. Rayment, A. Davenport, Atmospheric pitting corrosion of 304L stainless steel: The role of highly concentrated chloride solutions, Faraday Discuss., 180 (2015) 251-265. https://doi-org.sheffield.idm.oclc.org/10.1039/c4fd00246f

[5] C. Wang, F. Jiang, F. Wang, The characterization and corrosion resistance of cerium chemical conversion coatings for 304 stainless steel, Corros. Sci. 46 (2004) 75. https://doi-org.sheffield.idm.oclc.org/10.1016/S0010-938X(03)00135-5

[6] A. Galal, N.F. Atta, M.H.S. Al-Hassan, Effect of some thiophene derivatives on the electrochemical behavior of AISI 316 austenitic stainless steel in acidic solutions containing chloride ions I. Molecular structure and inhibition efficiency relationship, Mater. Chem. Phys. 89 (2005) 38–48. https://doi-org.sheffield.idm.oclc.org/10.1016/j.matchemphys.2004.08.019

[7] G. Salvago, G. Bollini, Localized corrosion probability in stainless steels after cathodic protection in seawater, Corrosion 54 (1999) 397. https://doi.org/10.5006/1.3284000

[8] K. Alvarez, S.K. Hyun, H. Tsuchiya, S. Fujimoto, H. Nakajima, Corrosion behaviour of Lotus-type porous high nitrogen nickel-free stainless steels, Corros. Sci. 50 (2008) 183–193. https://doi-org.sheffield.idm.oclc.org/10.1016/j.corsci.2007.06.004

[9] Y. Shi, B. Yang, P.K. Liaw, Corrosion-Resistant High-Entropy Alloys: A Review, Metals 7 (2017) 1-18. https://doi-org.sheffield.idm.oclc.org/10.3390/met7020043

[10] L.Q. Guo, Y. Bai, B.Z. Xu, W. Pan, J.X. Li, L.J. Qiao, Effect of hydrogen on pitting susceptibility of 2507 duplex stainless steel, Corros. Sci. 70 (2013) 140-144. https://doi-org.sheffield.idm.oclc.org/10.1016/j.corsci.2013.01.022

[11] M.D. Asaduzzaman, M.C. Mustafa, M. Islam, Effects of concentration of sodium chloride solution on the pitting corrosion behavior of AISI 304L austenitic stainless steel, Chem. Ind. Chem. Eng. Q. 17 (2011) 477-483. https://doi-org.sheffield.idm.oclc.org/10.2298/CICEQ110406032A

[12] E.J. Pickering, N.G. Jones, High-entropy alloys: a critical assessment of their founding principles and future prospects, Int. Mater. Rev. 61 (2016) 183-202. https://doi-org.sheffield.idm.oclc.org/10.1080/09506608.2016.1180020

[13] D.B. Miracle, O.N. Senkov, A critical review of high entropy alloys and related concepts, Acta Mater. 122 (2017) 448-511. https://doi-org.sheffield.idm.oclc.org/10.1016/j.actamat.2016.08.081

[14] J.W. Yeh, S.K. Chen, S.J. Lin, J.Y. Gan, T.S. Chin, T.T. Shun, C.H. Tsau, S.Y. Chang, Nanostructured High-Entropy Alloys with Multiple Principal Elements: Novel Alloy Design Concepts and Outcomes, Adv. Eng. Mater. 6 (2004) 299-303. https://doi-org.sheffield.idm.oclc.org/10.1002/adem.200300567

[15] C.L. Wu, S. Zhang, C.H. Zhang, H. Zhang, S.Y. Dong, Phase evolution and cavitation erosion-corrosion behavior of $FeCoCrAlNiTi_x$ high entropy alloy coatings on 304 stainless steel by laser surface alloying, J. Alloy. Compd. 698 (2017) 761-770. https://doi-org.sheffield.idm.oclc.org/10.1016/j.jallcom.2016.12.196

[16] J.W. Yeh, S.K. Chen, J.Y. Gan, S.J. Lin, T.S. Chin, T.T. Shun, C.H. Tsau, S.Y. Chang, Formation of simple crystal structures in Cu-Co-Ni-Cr-Al-Fe-Ti-V alloys with multiprincipal metallic elements, Metall. Mater. Trans. A 35 (2004) 2533-2536. https://doi-org.sheffield.idm.oclc.org/10.1007/s11661-006-0234-4

[17] S. Jiang, Z. Lin, H. Xu, Y. Sun, Studies on the microstructure and properties of $Al_xCoCrFeNiTi_{1-x}$ high entropy alloys, J. Alloy. Compd. 741 (2018) 826-833. https://doi-org.sheffield.idm.oclc.org/10.1016/j.jallcom.2018.01.247

[18] K.B. Zhang, Z.Y. Fu, J.Y. Zhang, J. Shi, W.M. Wang, H. Wang, Y.C. Wang, Q.J. Zhang, Annealing on the structure and properties evolution of the CoCrFeNiCuAl high-entropy alloy, J. Alloy. Compd. 502 (2010) 295-299. https://doi-org.sheffield.idm.oclc.org/10.1016/j.jallcom.2009.11.104

[19] O.N. Senkov, J.M. Scott, S.V. Senkova, D.B. Miracle, C. Woodward, Microstructure and room temperature properties of a high-entropy TaNbHfZrTi alloy, J. Alloy. Compd. 509 (2011) 6043-6048. https://doi-org.sheffield.idm.oclc.org/10.1016/j.jallcom.2011.02.171

[20] C. Ng, S. Guo, J. Luan, Q. Wang, J. Lu, S. Shi, C.T. Liu, Phase stability and tensile properties of Co-free $Al_{0.5}CrCuFeNi_2$ high-entropy alloys, J. Alloy. Comp. 584 (2014) 530-537. https://doi-org.sheffield.idm.oclc.org/10.1016/j.jallcom.2013.09.105

[21] B. Gorr, M. Azim, H.J. Christ, T. Mueller, D. Schliephake, M. Heilmaier, Phase equilibria, microstructure, and high temperature oxidation resistance of novel refractory high-entropy alloys, J. Alloy. Comp. 624 (2015) 270-278. https://doi-org.sheffield.idm.oclc.org/10.1016/j.jallcom.2014.11.012

[22] C.Y. Hsu, J.W. Yeh, S.K. Chen, T.T. Shun, Wear resistance and high-temperature compression strength of FCC CuCoNiCrAl0.5Fe alloy with boron addition, Metall. Mater. Trans. A 35 (2004) 1465-1469. https://doi-org.sheffield.idm.oclc.org/10.1007/s11661-004-0254-x

[23] Y.F. Kao, S.K. Chen, T.J. Chen, P.C. Chu, J.W. Yeh, S.J. Lin, Electrical, magnetic, and Hall properties of $Al_xCoCrFeNi$ high-entropy alloys, J. Alloy. Comp. 509 (2011) 1607-1614. https://doi-org.sheffield.idm.oclc.org/10.1016/j.jallcom.2010.10.210

[24] K.K. Alanemea, M.O. Bodunrina, S.R. Okea, Processing, alloy composition and phase transition effect on the mechanical and corrosion properties of high entropy alloys: a review, J. Mater. Res. Technol. 5 (2016) 384-393. https://doi-org.sheffield.idm.oclc.org/10.1016/j.jmrt.2016.03.004

[25] A. Rodriguez, J. Tylczak, M. Gao, P. Jablonski, M. Detrois, M. Ziomek-Moroz, J. Hawk, Effect of molybdenum on the corrosion behavior of high-entropy alloys $CoCrFeNi_2$ and $CoCrFeNi_2Mo_{0.25}$ under sodium chloride aqueous conditions, Adv. Mater. Sci. 2018 (2018) 1-11. https://doi-org.sheffield.idm.oclc.org/10.1155/2018/3016304

[26] Y.L. Chou, Y.C. Wang, J.W. Yeh, H.C. Shih, Pitting corrosion of the high-entropy alloy $Co_{1.5}CrFeNi_{1.5}Ti_{0.5}Mo_{0.1}$ in chloride-containing sulphate solutions, Corros. Sci. 52 (2010) 3481-3491. https://doi-org.sheffield.idm.oclc.org/10.1016/j.corsci.2010.06.025

[27] Y.J. Hsu, W.C. Chiang, J.K. Wu, Corrosion behavior of $FeCoNiCrCu_x$ high-entropy alloys in 3.5% sodium chloride solution, Mater. Chem. Phys. 92 (2005) 112-117. https://doi-org.sheffield.idm.oclc.org/10.1016/j.matchemphys.2005.01.001

[28] Y. Qiu, S. Thomas, M.A. Gibson, H.L. Fraser, N. Birbilis, Corrosion of high entropy alloys, npj Mat. Deg. 1 (2017) 1-18. https://doi.org/10.1038/s41529-017-0009-y

[29] T.M. Butler, M.L. Weaver, Oxidation behavior of arc melted AlCoCrFeNi multi-component high-entropy alloys, J. Alloy. Compd. 674 (2016) 229-244. https://doi-org.sheffield.idm.oclc.org/10.1016/j.jallcom.2016.02.257

[30] A. Munitz, S. Salhov, S. Hayun, N. Frage, Heat treatment impacts the micro-structure and mechanical properties of AlCoCrFeNi high entropy alloy, J. Alloy. Compd. 683 (2016) 221-230. https://doi-org.sheffield.idm.oclc.org/10.1016/j.jallcom.2016.05.034

[31] D.H. Xiao, P.F. Zhoua, W.Q. Wu, H.Y. Diao, M.C. Gao, M. Song, P.K. Liaw, Microstructure, mechanical and corrosion behaviors of AlCoCuFeNi-(Cr,Ti) high entropy alloys, Mater. Des. 116 (2017) 438-447. https://doi-org.sheffield.idm.oclc.org/ 10.1016/j.matdes.2016.12.036

[32] Y. Qiu, M.A. Gibson, H.L. Fraser, N. Birbilis, Corrosion characteristics of high entropy alloys, Mater. Sci. Technol. 31 (2015) 1235-1243. https://doi-org.sheffield.idm.oclc.org/ 10.1179/1743284715Y.0000000026

[33] Y. Shi, B. Yang, X. Xie, J. Brechtl, K. Dahmen, P. Liaw, Corrosion of $Al_xCoCrFeNi$ high-entropy alloys: Al-content and potential scan-rate dependent pitting behavior, Corros. Sci. 119 (2017) 33-45. https://doi-org.sheffield.idm.oclc.org/10.1016/j.corsci.2017.02.019

[34] W.R. Wang, W.L. Wang, J.W. Yeh, Phases, microstructure and mechanical properties of $Al_xCoCrFeNi$ high-entropy alloys at elevated temperatures, J. Alloy. Compd. 589 (2014) 143-152. https://doi-org.sheffield.idm.oclc.org/10.1016/j.jallcom.2013.11.084

[35] J. Cornide, M. Calvo-Dahlborg, S. Chambreland, L. Asensio Dominguez, Z. Leong, U. Dahlborg, A. Cunliffe, R. Goodall, I. Todd, Combined atom probe tomography and TEM

investigations of CoCrFeNi, CoCrFeNi-Pd_x (x = 0.5, 1.0, 1.5) and CoCrFeNi-Sn, Acta. Phys. Pol. A. 128 (2015) 557-560. https:// doi.org/10.12693/APhysPolA.128.557

[36] L. Liu, J.B. Zhu, C. Zhang, J.C. Li, Q. Jiang, Microstructure and the properties of FeCoCuNiSnx high entropy alloys, Mater. Sci. Eng., A. 548 (2012) 64-68. https://doi-org.sheffield.idm.oclc.org/10.1016/j.msea.2012.03.080

[37] Z.G. Zhu, K.H. Ma, Q. Wang, C.H. Shek, Compositional dependence of phase formation and mechanical properties in three CoCrFeNi-(Mn/Al/Cu) high entropy alloys, Intermetallics. 79 (2016) 1-11. https://doi-org.sheffield.idm.oclc.org/10.1016/j.intermet.2016.09.003

[38] P.M. Natishana, W.E. O'Gradyb, Chloride ion interactions with oxide-covered aluminum leading to pitting corrosion: A review, J. Electrochem. Soc. 161 (2014) 421-432. https://doi-org.sheffield.idm.oclc.org/10.1149/2.1011409jes

[39] P. Lopesino, J. Alcántara, D. de la Fuente, B. Chico, J.A. Jiménez, M. Morcillo, Corrosion of copper in unpolluted chloride-rich atmospheres, Metals. 8 (2018) 1-19. https://doi-org.sheffield.idm.oclc.org/10.3390/met8110866

[40] H. Cachet, F. Zenia, M. Froment, Corrosion-induced activation of SnO_2 films promoted by the electrochemical oxidation of chloride ions, J. Electrochem. Soc. 146 (1999) 977-983. https://doi-org.sheffield.idm.oclc.org/10.1149/1.1391708

[41] X. Zhong, G. Zhang, Y. Qiu, Z. Chen, X. Guo, C. Fu, The corrosion of tin under thin electrolyte layers containing chloride, Corros. Sci. 119 (2017) 33-45. https://doi-org.sheffield.idm.oclc.org/10.1016/j.corsci.2012.08.040

[42] A. Takeuchi, A. Inoue, Classification of bulk metallic glasses by atomic size difference, heat of mixing and period of constituent elements and its application to characterization of the main alloying element, Mater. Trans. 66 (2013) 14-25. https://doi.org/10.2320/matertrans.46.2817